Available online at www.sciencedirect.com
ScienceDirect
Comput. Methods Appl. Mech. Engrg. 364 (2020) 112981
Computer methods in applied mechanics and engineering
www.elsevier.com/locate/cma

Long-time simulation of the phase-field crystal equation using high-order energy-stable CSRK methods

Jaemin Shin[a], Hyun Geun Lee[b], June-Yub Lee[c,*]

[a] Department of Mathematics, Chungbuk National University, Cheongju 28644, Republic of Korea
[b] Department of Mathematics, Kwangwoon University, Seoul 01897, Republic of Korea
[c] Department of Mathematics, Ewha Womans University, Seoul 03760, Republic of Korea

Received 12 June 2019; received in revised form 9 February 2020; accepted 1 March 2020
Available online 16 March 2020

Abstract

The phase-field crystal (PFC) equation is derived by the gradient flow for the Swift–Hohenberg free energy functional; thus, the numerical method requires the energy of the functional to decrease. Convex Splitting Runge–Kutta (CSRK) methods can be suitably applied to achieve high-order temporal accuracy as well as unconditional energy stability and unique solvability. For the PFC equation, we prove the unconditional energy stability and unique solvability of the CSRK methods and provide one family of parameters of the second-order CSRK methods and possible examples of third-order CSRK methods. We present numerical experiments to demonstrate the accuracy and energy stability of the methods. Specifically, based on the high-order accuracy and energy stability of the CSRK method, we propose an indicator function capable of characterizing the pattern formation of the phase-field crystal model for long-time simulation.

Keywords: Phase-field crystal equation; High-order temporal accuracy; Unconditional energy stability; Convex Splitting Runge–Kutta method; Long-time simulation

1. Introduction

Phase-field models have emerged as a powerful computational approach for modeling and predicting morphological and microstructural evolution in materials at the mesoscale [1–3]. Many of these models attempt to minimize an energy functional $\mathcal{E}(\phi)$ by the gradient flow for $\mathcal{E}(\phi)$ in $\Omega \subset \mathbb{R}^d$ $(d = 1, 2, 3)$,

$$\frac{\partial \phi}{\partial t} = -\text{grad}\ \mathcal{E}(\phi), \tag{1}$$

where the symbol "grad" denotes the gradient in the sense of the Gâteaux derivative. It is worth noting that the energy functional $\mathcal{E}(\phi)$ is non-increasing in time because (1) is of the gradient type. The phase-field crystal (PFC) equation has been suggested to study the microstructural evolution of two-phase systems in terms of their atomic length and diffusive time scales [4,5]. The PFC equation,

$$\frac{\partial \phi}{\partial t} = \Delta\left(\phi^3 - \epsilon\phi + (1+\Delta)^2\phi\right), \tag{2}$$

* Corresponding author.
E-mail address: jyllee@ewha.ac.kr (J.-Y. Lee).

https://doi.org/10.1016/j.cma.2020.112981
0045-7825/

can be represented by the gradient flow for the Swift–Hohenberg type free energy functional [3],

$$\mathcal{E}(\phi) = \int_{\Omega} \left(\frac{1}{4}\phi^4 + \frac{1}{2}\phi \left(-\epsilon + (1+\Delta)^2 \right) \phi \right) d\mathbf{x}, \tag{3}$$

where ϕ is the conserved density field and ϵ is a positive bifurcation constant with physical significance. Here, we assume that ϕ is periodic on Ω. The main difficulty that has to be overcome when developing a numerical method based on the PFC equation (2) is the severe stability restriction on the time step owing to the nonlinear and sixth-order differential terms. Thus, obtaining analytic or numerical solutions by certain elementary methods is generally challenging.

Many remarkable second-order methods for the PFC equation (2) have been proposed to overcome the time step restriction and guarantee energy stability. In this regard, a possibility is to extend the first-order convex splitting (CS) method [6], which is based on splitting the energy functional $\mathcal{E}(\phi)$ into two convex functionals, $\mathcal{E}(\phi) = \mathcal{E}_c(\phi) - \mathcal{E}_e(\phi)$. For example, a combination of the secant-type scheme and an extrapolation was presented [7–9], a modified Crank–Nicolson method was considered [10], and backward difference was employed [11]. On the other hand, several methods that obviated the need for splitting have been developed. Invariant energy quadratization was employed to develop efficient linear schemes [12]. Zhang et al. [13] developed an unconditionally energy stable scheme by using the secant-type difference with an adaptive time stepping strategy. Gomez and Nogueira [14] proposed a nonlinear, second-order time accurate, and unconditionally gradient stable method with the modified Crank–Nicolson method.

Recently, we proposed the Convex Splitting Runge–Kutta (CSRK) method [8,15] which provides, in the abstract sense, high-order temporal accuracy and unconditional energy stability with appropriate RK coefficients. In this study, we adopt the CSRK method for the PFC equation (2) to obtain high-order accurate and energy stable numerical solutions of (2). For the PFC equation, we prove the unconditional energy stability and unique solvability of the CSRK methods and provide one family of parameters for the second-order CSRK methods and possible examples of third-order CSRK methods. We present numerical examples to verify the accuracy and energy stability of the CSRK methods. In addition, we propose an indicator function by using the high-order energy stable CSRK method, and using the indicator function we confirm that the PFC equation generates different patterns, such as striped or hexagonal, depending on the values of ϵ and $\bar{\phi}$.

In Section 2, we briefly describe the CSRK method with a resemble design and provide the RK coefficients for second- and third-order accuracy. Numerical experiments showing the accuracy and stability of the proposed methods are presented in Section 3. In particular, we propose the indicator function to characterize the patterns of the PFC model for the long-time simulation in Section 3.3. Finally, conclusions are drawn in Section 4.

2. Numerical method

We begin by considering the convex splitting of the energy functional (3),

$$\mathcal{E}_c(\phi) = \int_{\Omega} \left(\frac{1}{4}\phi^4 + \frac{1}{2}\phi(1+\Delta)^2\phi \right) d\mathbf{x}, \quad \mathcal{E}_e(\phi) = \int_{\Omega} \frac{\epsilon}{2}\phi^2 d\mathbf{x}, \tag{4}$$

which we previously used [8,15]. In general, the CSRK method allusively indicates that we can consider another splitting, for example, CS as used in [7,16] is also highly applicable. However, in this paper, we present high-order energy stable methods that only use the splitting in (4). To keep the explanation simple, we define functions as

$$\Psi(\phi) = \frac{1}{4}\phi^4 - \frac{\epsilon}{2}\phi^2, \quad \Psi_c(\phi) = \frac{1}{4}\phi^4, \quad \Psi_e(\phi) = \frac{\epsilon}{2}\phi^2, \tag{5}$$

where $\Psi(\phi) = \Psi_c(\phi) - \Psi_e(\phi)$. Note that both functions $\Psi_c(\phi)$ and $\Psi_e(\phi)$ are convex functions.

First, we set a zero-stage as $\phi_0 = \phi^n$. For each stage $i = 1, 2, \ldots, s$, we calculate

$$\phi_i = \phi_0 + \Delta t \sum_{j=1}^{i} r_{ij} \Delta \left(\Psi_c'(\phi_j) - \Psi_e'(\phi_{j-1}) + (1+\Delta)^2 \phi_j \right), \tag{6}$$

where the coefficients in (6) can be represented by a lower triangular matrix

$$\mathbf{R} = \begin{pmatrix} r_{11} & 0 & \cdots & 0 \\ r_{21} & r_{22} & \cdots & 0 \\ \vdots & \vdots & \ddots & \vdots \\ r_{s1} & r_{s2} & \cdots & r_{ss} \end{pmatrix}. \tag{7}$$

Finally, we evaluate the next time approximation as $\phi^{n+1} = \phi_s$. Now, we refer to the proposed method (6) with the matrix $\mathbf{R}$ as the CSRK-$\mathbf{R}$ method.

To ensure the simplicity of the proof in the following sections, we rewrite the CSRK-$\mathbf{R}$ method (8) with auxiliary variables μ_j as

$$\begin{aligned} \phi_i - \phi_0 &= \Delta t \sum_{j=1}^{i} r_{ij} \Delta \mu_j, \\ \mu_j &= \Psi_c'(\phi_j) - \Psi_e'(\phi_{j-1}) + (1+\Delta)^2 \phi_j. \end{aligned} \tag{8}$$

2.1. Unique solvability

Lemma 1 (*Mass Conservation*)**.** *The CSRK-*$\mathbf{R}$ *scheme (8) is mass conserving.*

Proof. The mass conservation of (8) follows from

$$(\phi_i - \phi_0, \mathbf{1})_{L^2} = \Delta t \sum_{j=1}^{i} r_{ij} \left(\Delta \mu_j, \mathbf{1}\right)_{L^2} = -\Delta t \sum_{j=1}^{i} r_{ij} \left(\nabla \mu_j, \nabla \mathbf{1}\right)_{L^2} = 0, \tag{9}$$

where $(\phi, \psi)_{L^2} = \int_\Omega \phi\psi \, d\mathbf{x}$ denotes the L^2-inner product. Here, the integration by parts formula can be derived for ϕ and ψ such that the periodic boundary conditions are satisfied,

$$(\phi, \Delta\psi)_{L^2} = -(\nabla\phi, \nabla\psi)_{L^2}. \tag{10}$$

Thus, if (8) has a solution ϕ_i, then it must be $(\phi_i, \mathbf{1})_{L^2} = (\phi_0, \mathbf{1})_{L^2}$ for any i. □

Now, we consider the Hilbert space H_0 as a zero average space. For given $v_1, v_2 \in H_0$, we define the inner product of the dual space by $(v_1, v_2)_{H^{-1}} = \left(\nabla\varphi_{v_1}, \nabla\varphi_{v_2}\right)_{L^2}$, where $\varphi_{v_1}, \varphi_{v_2} \in H_0$ are the solutions of the periodic boundary value problem $-\Delta\varphi_{v_1} = v_1$ and $-\Delta\varphi_{v_2} = v_2$ in Ω. From the above definition, if $\psi \in H_0$, then we have the identity

$$(-\Delta\phi, \psi)_{H^{-1}} = (\phi, \psi)_{L^2}. \tag{11}$$

The identity (11) is subsequently used to prove the solvability of the proposed method.

Theorem 2 (*Unique Solvability*)**.** *Suppose that ϕ is sufficiently regular. The proposed CSRK-*$\mathbf{R}$ *scheme (8) is uniquely solvable for any time step size $\Delta t > 0$, provided that $r_{ii} \geq 0$ for all i.*

Proof. For each stage $i = 1, 2, \ldots, s$, we need to solve

$$\phi_i - r_{ii}\Delta t \Delta\left(\Psi_c'(\phi_i) + (1+\Delta)^2 \phi_i\right) = \phi_0 + \Delta t \, S_i, \tag{12}$$

where

$$S_i = \sum_{j=1}^{i-1} r_{ij} \Delta\left(\Psi_c'(\phi_j) + (1+\Delta)^2 \phi_j\right) - \sum_{j=1}^{i} r_{ij} \Delta \Psi_e'(\phi_{j-1}). \tag{13}$$

Let us consider the following functional defined on $\widetilde{H} = \left\{\phi \mid (\phi, \mathbf{1})_{L^2} = (\phi_0, \mathbf{1})_{L^2}\right\}$:

$$Q(\phi) = \frac{1}{2}\|\phi - \phi_0\|_{H^{-1}}^2 + r_{ii}\Delta t \left(\Psi_c(\phi) + \frac{1}{2}((1+\Delta)\phi)^2, \mathbf{1}\right)_{L^2} - \Delta t \, (S_i, \phi)_{H^{-1}}. \tag{14}$$

Suppose that ψ and $\Delta\psi$ are sufficiently regular with $\psi \in H_0$. The first variation is calculated as

$$\begin{aligned}\frac{dQ}{d\eta}(\phi+\eta\psi)\Big|_{\eta=0} &= (\phi-\phi_0,\psi)_{H^{-1}} + r_{ii}\Delta t\left(\Psi_c'(\phi)+(1+\Delta)^2\phi,\psi\right)_{L^2} - \Delta t\,(S_i,\psi)_{H^{-1}}.\\ &= \left(\phi-\phi_0-r_{ii}\Delta t\Delta\left(\Psi_c'(\phi)+(1+\Delta)^2\phi\right)-\Delta t S_i,\psi\right)_{H^{-1}}.\end{aligned} \tag{15}$$

Next, calculation of the second variation reveals

$$\frac{d^2Q}{d\eta^2}(\phi+\eta\psi)\Big|_{\eta=0} = \|\psi\|^2_{H^{-1}} + r_{ii}\Delta t\left(\Psi_c'(\phi)+(1+\Delta)^2\phi,\psi\right)_{L^2} \geq 0, \tag{16}$$

which implies that $Q(\phi)$ is a convex functional. Thus, it has a unique minimizer $\phi_i \in \widetilde{H}$. At the unique minimizer for each stage, $\frac{dQ}{d\eta}(\phi_i+\eta\psi)\Big|_{\eta=0} = 0$; thus, (12) has a unique solution ϕ_i. Therefore, the proposed scheme (8) is uniquely solvable for any time step size $\Delta t > 0$. □

2.2. Unconditional energy stability

We provide two lemmas before we present a condition to render the proposed CSRK-**R** scheme (8) unconditionally energy stable.

Lemma 3. *If $\Psi(\phi)$ can be split into $\Psi(\phi) = \Psi_c(\phi) - \Psi_e(\phi)$, where both functions $\Psi_c(\phi)$ and $\Psi_e(\phi)$ are convex, then*

$$\Psi(\phi) - \Psi(\psi) \leq \left(\Psi_c'(\phi) - \Psi_e'(\psi)\right)(\phi-\psi). \tag{17}$$

Proof. We refer to previous work [8,16] for the proof of this lemma. □

Lemma 4. *We have the following equality:*

$$\int_\Omega \left(\llbracket\phi\rrbracket_m^n (1+\Delta)^2\phi_n - \tfrac{1}{2}\left[\!\left[((1+\Delta)\phi)^2\right]\!\right]_m^n\right)d\mathbf{x} = \tfrac{1}{2}\int_\Omega \left((1+\Delta)\llbracket\phi\rrbracket_m^n\right)^2 d\mathbf{x}, \tag{18}$$

where we define the difference operator by $\llbracket\phi\rrbracket_m^n = \phi_n - \phi_m$.

Proof.

$$\begin{aligned}\int_\Omega \llbracket\phi\rrbracket_m^n (1+\Delta)^2\phi_n\,d\mathbf{x} &= \int_\Omega \llbracket\phi\rrbracket_m^n (1+\Delta)^2\left(\frac{\phi_n+\phi_m}{2}+\frac{\llbracket\phi\rrbracket_m^n}{2}\right)d\mathbf{x}\\ &= \tfrac{1}{2}\int_\Omega (1+\Delta)^2\left[\!\left[\phi^2\right]\!\right]_m^n d\mathbf{x} + \tfrac{1}{2}\int_\Omega \llbracket\phi\rrbracket_m^n (1+\Delta)^2\llbracket\phi\rrbracket_m^n d\mathbf{x}\\ &= \tfrac{1}{2}\int_\Omega \left[\!\left[((1+\Delta)\phi)^2\right]\!\right]_m^n d\mathbf{x} + \tfrac{1}{2}\int_\Omega \left((1+\Delta)\llbracket\phi\rrbracket_m^n\right)^2 d\mathbf{x}\end{aligned} \tag{19}$$

Rearranging (19), we have the equality. □

Positive definite condition. *The CSRK-**R** method (8) is said to satisfy the positive definite condition if a row difference matrix $\widetilde{\mathbf{R}}$ is positive definite after a symmetric transformation, where $\widetilde{\mathbf{R}} = \mathbf{R} - S\mathbf{R}$ is defined as follows with a shift matrix $S_{ij} = \delta_{i,j+1}$,*

$$\widetilde{\mathbf{R}} = \begin{pmatrix}\tilde r_{11} & 0 & \cdots & 0\\ \tilde r_{21} & \tilde r_{22} & \cdots & 0\\ \vdots & \vdots & \ddots & \vdots\\ \tilde r_{s1} & \tilde r_{s2} & \cdots & \tilde r_{ss}\end{pmatrix} = \begin{pmatrix} r_{11} & 0 & \cdots & 0\\ r_{21} & r_{22} & \cdots & 0\\ \vdots & \vdots & \ddots & \vdots\\ r_{s1} & r_{s2} & \cdots & r_{ss}\end{pmatrix} - \begin{pmatrix} 0 & 0 & \cdots & 0\\ r_{11} & 0 & \cdots & 0\\ \vdots & \vdots & \ddots & \vdots\\ r_{s-1,1} & r_{s-1,2} & \cdots & 0\end{pmatrix}. \tag{20}$$

Theorem 5 (*Unconditional Energy Stability*)**.** *If the CSRK-**R** method (8) satisfies the positive definite condition, then it is unconditionally energy stable, meaning that $\mathcal{E}\left(\phi^{n+1}\right) \leq \mathcal{E}(\phi^n)$, for any time step size $\Delta t > 0$.*

Proof. The difference between the two adjacent stages can be calculated as

$$[\![\phi]\!]_{i-1}^{i} = \Delta t \sum_{j=1}^{i} \tilde{r}_{ij} \Delta\mu_j, \tag{21}$$

for all i. By Lemma 3, the energy difference between two adjacent stages is

$$[\![\mathcal{E}(\phi)]\!]_{i-1}^{i} \le \int_{\Omega} \left(\left(\Psi_c'(\phi_i) - \Psi_e'(\phi_{i-1}) \right) [\![\phi]\!]_{i-1}^{i} + \tfrac{1}{2} \left[\!\left[((1+\Delta)\phi)^2 \right]\!\right]_{i-1}^{i} \right) d\mathbf{x}. \tag{22}$$

From the definition of μ_j, we have

$$[\![\mathcal{E}(\phi)]\!]_{i-1}^{i} \le \int_{\Omega} \left(\left(\mu_i - (1+\Delta)^2 \phi_i \right) [\![\phi]\!]_{i-1}^{i} + \tfrac{1}{2} \left[\!\left[((1+\Delta)\phi)^2 \right]\!\right]_{i-1}^{i} \right) d\mathbf{x}. \tag{23}$$

By Lemma 4,

$$[\![\mathcal{E}(\phi)]\!]_{i-1}^{i} \le \int_{\Omega} \left(\mu_i [\![\phi]\!]_{i-1}^{i} - \tfrac{1}{2} \left((1+\Delta) [\![\phi]\!]_{i-1}^{i} \right)^2 \right) d\mathbf{x} \le \int_{\Omega} \mu_i [\![\phi]\!]_{i-1}^{i} \, d\mathbf{x}. \tag{24}$$

After summation, we have

$$[\![\mathcal{E}(\phi)]\!]_{0}^{s} = \sum_{i=1}^{s} [\![\mathcal{E}(\phi)]\!]_{i-1}^{i} \le \sum_{i=1}^{s} \int_{\Omega} \mu_i [\![\phi]\!]_{i-1}^{i} \, d\mathbf{x} = -\Delta t \int_{\Omega} (\nabla\boldsymbol{\mu})^T \widetilde{\mathbf{R}} \, (\nabla\boldsymbol{\mu}) \, d\mathbf{x}, \tag{25}$$

where $\nabla\boldsymbol{\mu} = (\nabla\mu_1, \ldots, \nabla\mu_s)^T$. Because $\widetilde{\mathbf{R}}$ is positive definite, $[\![\mathcal{E}(\phi)]\!]_0^s \le 0$. It follows that the energy dissipation is satisfied, $\mathcal{E}\left(\phi^{n+1}\right) = \mathcal{E}(\phi_s) \le \mathcal{E}(\phi_0) = \mathcal{E}(\phi^n)$. □

Remark 1. With the convex splitting (4), we can consider a well-known first-order CS method

$$\frac{\phi^{n+1} - \phi^n}{\Delta t} = \Delta \left((\phi^{n+1})^3 + (1+\Delta)^2 \phi^{n+1} \right) - \epsilon \Delta \phi^n. \tag{26}$$

The energy stability is easily explained because the CSRK-**R** method (8) constructs the CS method (26) with a resemble base matrix $\mathbf{R} = (1)$. The corresponding row difference matrix $\widetilde{\mathbf{R}} = (1)$ is positive definite, such that the CS method (26) guarantees the energy dissipation property, $\mathcal{E}\left(\phi^{n+1}\right) \le \mathcal{E}(\phi^n)$.

2.3. Resemble matrices for high-order accuracy

With the resemble base matrix (7), the CSRK-**R** method can be represented by the two-additive Runge–Kutta method with Butcher tableaus:

$$\begin{array}{c|c} \mathbf{c} & \mathbf{A} \\ \hline & \mathbf{b}^T \end{array} = \begin{array}{c|cccccc} 0 & 0 & 0 & 0 & \cdots & 0 \\ c_1 & 0 & r_{11} & 0 & \cdots & 0 \\ c_2 & 0 & r_{21} & r_{22} & \cdots & 0 \\ \vdots & \vdots & \vdots & \vdots & \ddots & \vdots \\ c_s & 0 & r_{s1} & r_{s2} & \cdots & r_{ss} \\ \hline & 0 & r_{s1} & r_{s2} & \cdots & r_{ss} \end{array}, \quad \begin{array}{c|c} \hat{\mathbf{c}} & \hat{\mathbf{A}} \\ \hline & \hat{\mathbf{b}}^T \end{array} = \begin{array}{c|cccccc} 0 & 0 & 0 & 0 & \cdots & 0 \\ c_1 & r_{11} & 0 & 0 & \cdots & 0 \\ c_2 & r_{21} & r_{22} & 0 & \cdots & 0 \\ \vdots & \vdots & \vdots & \vdots & \ddots & \vdots \\ c_s & r_{s1} & r_{s2} & \cdots & r_{ss} & 0 \\ \hline & r_{s1} & r_{s2} & \cdots & r_{ss} & 0 \end{array}, \tag{27}$$

where $\mathbf{c} = \mathbf{A}\mathbf{1}$ and $\hat{\mathbf{c}} = \hat{\mathbf{A}}\mathbf{1}$. Table 1 lists the order conditions under which two-additive Runge–Kutta methods have first-, second-, and third-order accuracy if $\mathbf{c} = \hat{\mathbf{c}}$. A simple description of the order conditions is presented in our previous work [17], in which only Taylor's expansion is used. The reader is also referred to other explanations of the order condition [18–20] and references therein.

Note that $\mathbf{b} \cdot \mathbf{1} = 1$ and $\hat{\mathbf{b}} \cdot \mathbf{1} = 1$ are identical by the resemble design. In summary, we have 1 condition for first-order accuracy, 3 conditions for second-order accuracy, and 9 conditions for third-order accuracy.

We now introduce a few examples of the resemble base matrix $\mathbf{R}$ such that $\widetilde{\mathbf{R}}$ is positive definite. First, $\mathbf{R}_1 = (1)$ is a trivial matrix with first-order accuracy. Next, we consider the three-stage method because two-stage resemble

Table 1
Order conditions of two-additive RK methods up to third-order accuracy.

Order	Stand-alone conditions		Coupling conditions
1	$\mathbf{b}\cdot\mathbf{1}=1$	$\hat{\mathbf{b}}\cdot\mathbf{1}=1$	–
2	$\mathbf{b}\cdot\mathbf{c}=1/2$	$\hat{\mathbf{b}}\cdot\mathbf{c}=1/2$	–
3	$\mathbf{b}\cdot\mathbf{c}^2=1/3$ $\mathbf{b}\cdot\mathbf{A}\mathbf{c}=1/6$	$\hat{\mathbf{b}}\cdot\mathbf{c}^2=1/3$ $\hat{\mathbf{b}}\cdot\hat{\mathbf{A}}\mathbf{c}=1/6$	$\mathbf{b}\cdot\hat{\mathbf{A}}\mathbf{c}=\hat{\mathbf{b}}\cdot\mathbf{A}\mathbf{c}=1/6$

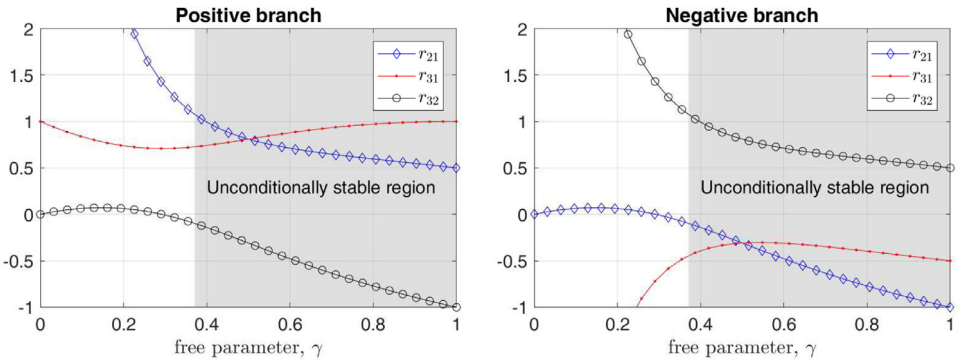

Fig. 1. Coefficients of the resemble base matrix for second-order accuracy.

methods with second-order accuracy do not exist. To enable the convenient design of tables, we consider a type of singly diagonal matrix,

$$\mathbf{R}_2(\gamma)=\begin{pmatrix}\gamma & 0 & 0\\ r_{21} & \gamma & 0\\ r_{31} & r_{32} & \gamma\end{pmatrix}. \tag{28}$$

Using this matrix (28), we construct RK tables $(\mathbf{A},\mathbf{b},\mathbf{c})$ and $\left(\hat{\mathbf{A}},\hat{\mathbf{b}},\hat{\mathbf{c}}\right)$ and solve the nonlinear equations by using the order conditions in Table 1 up to second-order accuracy. As a result, we have

$$r_{21}=\frac{\left(\frac{1}{2}-\gamma^2\right)\pm\sqrt{D}}{2\gamma},\quad r_{32}=p_2/r_{21},\quad r_{31}=p_1-r_{32}, \tag{29}$$

where $D=1/4-3\gamma^2+8\gamma^3-3\gamma^4$, $p_1=1-\gamma$, and $p_2=1/2-2\gamma+\gamma^2$. Fig. 1 shows the coefficients in $\mathbf{R}_2$ with respect to γ for second-order accuracy. The shaded region indicates the area in which $\left(\widetilde{\mathbf{R}}_2+\widetilde{\mathbf{R}}_2^T\right)/2$ is positive definite, which implies that the methods in this region are unconditionally energy stable. We carried out the numerical test of the second-order method, CSRK-$\mathbf{R}_2$ by using the coefficients in the negative branch.

For third-order accuracy, an example of the resemble base matrix $\mathbf{R}_3(\gamma)$ is

$$\mathbf{R}_3\left(\tfrac{1}{2}\right)=\begin{pmatrix}
\frac{1}{2} & 0 & 0 & 0 & 0 & 0\\
\frac{1}{2} & \frac{1}{2} & 0 & 0 & 0 & 0\\
-\frac{1}{10} & \frac{1}{10} & \frac{1}{2} & 0 & 0 & 0\\
\frac{13252051}{50981620} & -\frac{100507933}{407852960} & \frac{19290953}{81570592} & \frac{1}{2} & 0 & 0\\
\frac{401851541}{5098162000} & -\frac{20327867}{637270250} & -\frac{200790581}{1019632400} & \frac{1}{20} & \frac{1}{2} & 0\\
\frac{3217}{14300} & -\frac{703}{7150} & -\frac{6359}{42900} & -\frac{4556}{10725} & \frac{406}{429} & \frac{1}{2}
\end{pmatrix} \tag{30}$$

which we previously introduced [21]. Here, we provide two more examples with different parameters of γ on the diagonal,

$$\mathbf{R}_3\left(\tfrac{1}{3}\right) = \begin{pmatrix} 0.3333 & 0 & 0 & 0 & 0 & 0 \\ 0.3964 & 0.3333 & 0 & 0 & 0 & 0 \\ -0.1321 & 0.0986 & 0.3333 & 0 & 0 & 0 \\ 0.1087 & -0.1559 & 0.3141 & 0.3333 & 0 & 0 \\ 0.3622 & -0.2153 & -0.0059 & 0.0032 & 0.3333 & 0 \\ 0.3622 & -0.1853 & 0.0667 & -0.3330 & 0.7561 & 0.3333 \end{pmatrix}, \tag{31}$$

and

$$\mathbf{R}_3\left(\tfrac{2}{3}\right) = \begin{pmatrix} 0.6667 & 0 & 0 & 0 & 0 & 0 \\ 0.2792 & 0.6667 & 0 & 0 & 0 & 0 \\ -0.3021 & 0.1016 & 0.6667 & 0 & 0 & 0 \\ 0.3502 & -0.4133 & 0.2391 & 0.6667 & 0 & 0 \\ -0.1113 & 0.1801 & -0.3918 & 0.0540 & 0.6667 & 0 \\ 0.1665 & -0.3754 & -0.5506 & -0.2258 & 1.3186 & 0.6667 \end{pmatrix}, \tag{32}$$

which are rounded to four decimal places. The methods corresponding to (30)–(32) satisfy the positive definite because the minimum eigenvalue of $\left(\widetilde{\mathbf{R}}_3 + \widetilde{\mathbf{R}}_3^T\right)/2$ is approximately 0.0063, 0.0057, and 0.0255, respectively. Furthermore, it is easy to verify that the coefficients induced by $\mathbf{R}_3$ satisfy the order conditions in Table 1 up to third-order accuracy. These examples imply that many other cases satisfy the high-order accuracy and energy stability. We note that the existence of a third-order table with fewer than six stages is yet to be reported and the choice of the best coefficient matrices depends on the specific problem.

3. Numerical experiments

In this section, we present numerical results to validate the efficiency and accuracy of the proposed schemes. We choose the periodic boundary conditions and use the Fourier spectral method to discretize the variables in space. We note that the periodic boundary conditions are relevant in the study of PFC.

Because (8) is a nonlinear system, we need a nonlinear iterative solver. For the ith stage, we can rewrite the equation as (12),

$$\phi_i - r_{ii}\Delta t\Delta\left(\Psi_c'(\phi_i) + (1+\Delta)^2\phi_i\right) = S_i. \tag{33}$$

By applying a linearization $\Psi_c'(\phi_i) \approx \Psi_c'(\phi_{i,m}) + \Psi_c''(\phi_{i,m})(\phi_{i,m+1} - \phi_{i,m})$, we have a Newton-type nonlinear iterative method as

$$\mathcal{L}(\phi_{i,m+1}) = S_i + r_{ii}\Delta t\Delta\left(\Psi_c''(\phi_{i,m})\phi_{i,m} - \Psi_c'(\phi_{i,m})\right), \tag{34}$$

where $\mathcal{L}(\phi) = \left(I - r_{ii}\Delta t\Delta\left(\Psi_c''(\phi_{i,m}) + (1+\Delta)^2\right)\right)\phi$. The nonlinear iterations (34) can also be used until the relative l_2-norm of the consecutive error of $\phi_{i,m+1}$ is less than tol. Then let ϕ_i be the limiting value of $\phi_{i,m+1}$. Owing to the Newton-type nonlinear iterative method, the maximum number of iterative cycles was less than or equal to 6 in the entire numerical simulations with $tol = 10^{-6}$.

3.1. Numerical convergence tests with smooth initial data in 2D

We demonstrate the numerical convergence of the CSRK methods when solving the PFC equation with the periodic boundary condition on the domain $\Omega = [0, 32] \times [0, 32]$. For the convergence test of the time accuracy, we consider the initial condition

$$\phi(x, y, 0) = 0.03 + 0.005\sum_{l=0}^{6}\sum_{m=0}^{6}\mathrm{Re}\left[a_{lm}e^{\frac{2\pi i}{32}(lx)}\right]\cdot\mathrm{Re}\left[b_{lm}e^{\frac{2\pi i}{32}(my)}\right], \tag{35}$$

where a_{lm} and b_{lm} are random complex numbers with $\|a_{lm}\|_\infty \le 1$ and $\|b_{lm}\|_\infty \le 1$. For each frequency l and m, there are four different modes $\cos(l\xi_x)\cos(m\xi_y)$, $\cos(l\xi_x)\sin(m\xi_y)$, $\sin(l\xi_x)\cos(m\xi_y)$, and $\sin(l\xi_x)\sin(m\xi_y)$ where $(\xi_x, \xi_y) \in [0, 2\pi] \times [0, 2\pi]$. We can have all of these four modes by choosing random complex coefficients, a_{lm} and

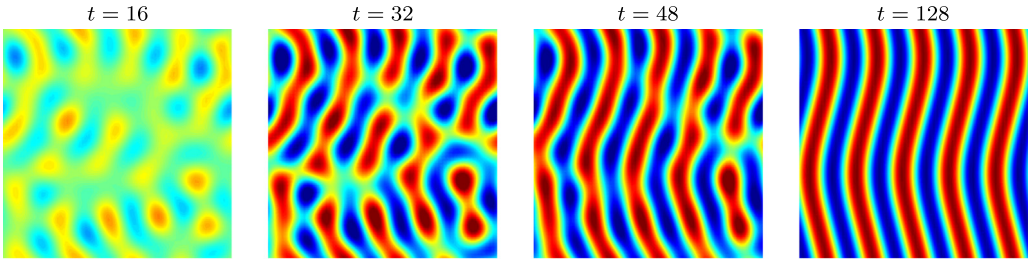

Fig. 2. Solution evolutions with smooth initial condition in 2D. (For interpretation of the references to color in this figure legend, the reader is referred to the web version of this article.)

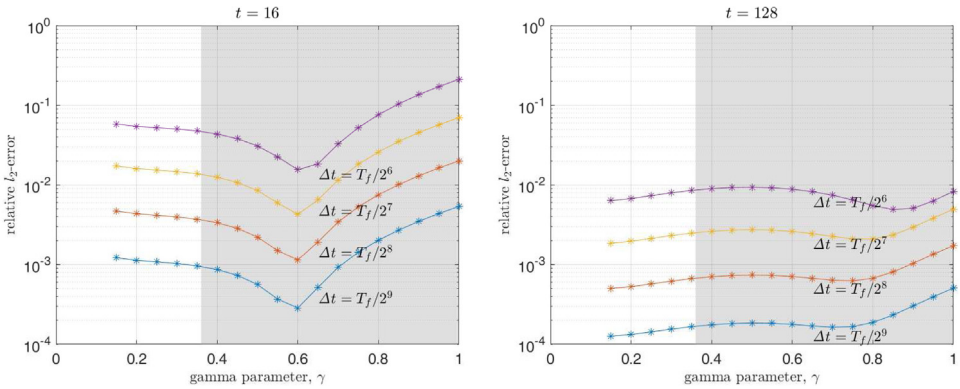

Fig. 3. Relative l_2-error of CSRK-$\mathbf{R}_2$ (γ).

b_{lm}. All of these modes are relatively smooth function and numerically well-resolved on the computational grid with $\Delta x = \Delta y = 1/2$ or $\Delta\xi_x = \Delta\xi_y = \pi/32$, therefore we can consider (35) as the smooth initial condition with all possible 49 ($= 7 \times 7$) low frequency modes. For the numerical simulations, $\epsilon = 0.2$ is used and the numerical solution evolves to time $T_f = 128$.

Fig. 2 shows the time evolution of the solution with a sufficiently small time step $\Delta t = T_f/2^{14}$ using the third-order method, CSRK-$\mathbf{R}_3(1/3)$. In each figure, the red, green, and blue regions indicate $\phi = 1$, 0, and -1, respectively.

Fig. 3 shows the relative l_2-norm errors when varying parameter γ with different time steps $\Delta t = T_f/2^9$, $T_f/2^8$, $T_f/2^7$, and $T_f/2^6$. For the numerical simulation, we used the second-order methods in the negative branch and executed the computation by increasing γ in increments of 0.05. The numerical solutions with $\gamma \lesssim 0.15$ blow up and are not marked in this figure; otherwise, the displayed results are numerically energy-stable. Furthermore, the shaded region demarcates the area in which the unconditional energy stability is guaranteed as in Fig. 1. Fig. 3 indicates that the accuracy can depend on various situations; hence, we selected $\gamma = 4/5$ for our numerical tests.

Fig. 4 shows the relative l_2-errors for the numerical solution of the methods corresponding to (30)–(32) with various $\Delta t = T_f/2^{11}, T_f/2^{10}, \ldots, T_f/2^3$. Here, the errors are computed in comparison with a quadruply over-resolved reference numerical solution obtained using CSRK-$\mathbf{R}_3(1/3)$. We observe that all the methods show third-order convergence.

Fig. 5 shows the relative l_2-errors for the numerical solution with various $\Delta t = T_f/2^{11}, T_f/2^{10}, \ldots, T_f/2^3$. Here, the errors are computed in comparison with a quadruply over-resolved reference numerical solution obtained using CSRK-$\mathbf{R}_3(1/3)$. The results show that the CSRK methods yield the desired order accuracy in time.

3.2. Energy dissipation test with randomly initial data in 2D

We demonstrate the numerical convergence of the CSRK methods for solving the PFC equation with the periodic boundary condition with the following initial condition

$$\phi(x, y, 0) = 0.1 + 0.05 \cdot \mathrm{rand}(x, y) \tag{36}$$

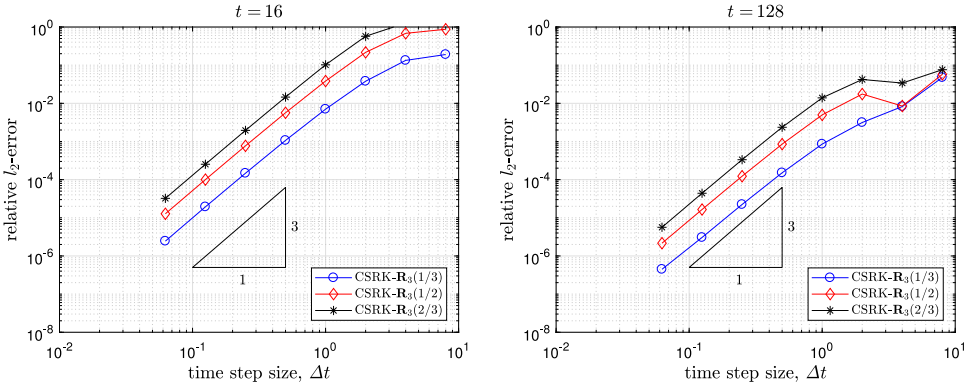

Fig. 4. Relative l_2-error of CSRK-$\mathbf{R}_3(\gamma)$ for various γ.

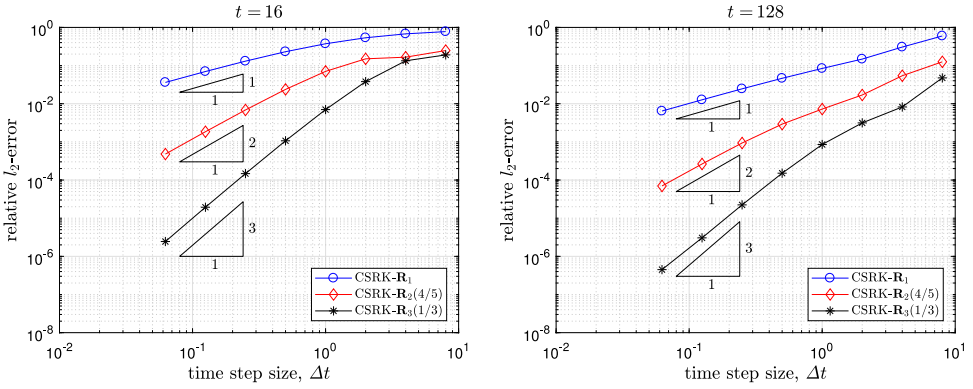

Fig. 5. Relative l_2-error for various CSRK-**R** methods.

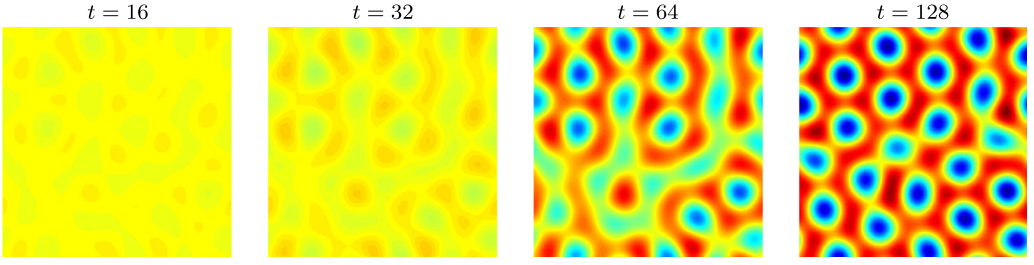

Fig. 6. Solution evolutions with random initial condition in 2D. (For interpretation of the references to color in this figure legend, the reader is referred to the web version of this article.)

on the domain $\Omega = [0, 32] \times [0, 32]$. Here, rand (x, y) is a uniformly random number between -1 and 1. For the numerical simulations, $\epsilon = 0.1$ is used and the grid size is fixed to $\Delta x = \Delta y = 1/2$, which provides sufficient spatial accuracy. The numerical solution evolves to time $T_f = 128$.

Fig. 6 shows the time evolution of the solution with a sufficiently small time step $\Delta t = T_f/2^{14}$ using the third-order method, CSRK-$\mathbf{R}_3(1/3)$. In each figure, the red, green, and blue regions indicate $\phi = 1$, 0, and -1, respectively.

Fig. 7 shows the evolution of the energy functional for the numerical solution with various time steps $\Delta t = T_f/2^6, T_f/2^5, T_f/2^4, T_f/2^3$. The solid line indicates the energy evolution of the reference solution. All curves are non-increasing in time and the higher method is close to the reference line.

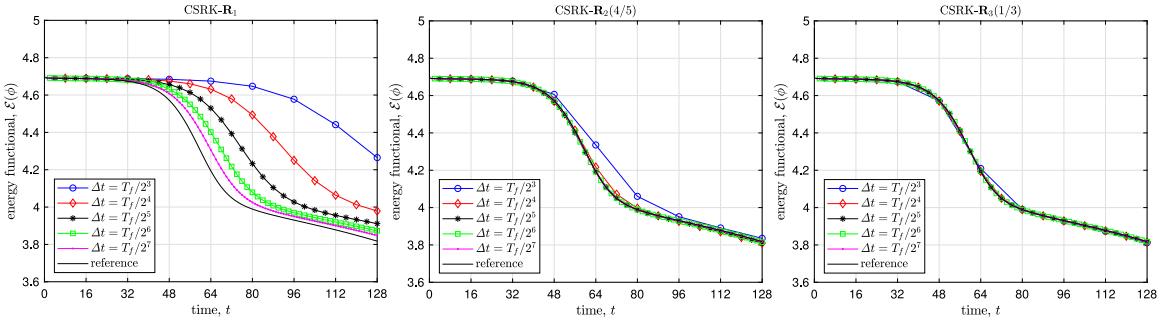

Fig. 7. Evolution of energy functional $\mathcal{E}(\phi)$.

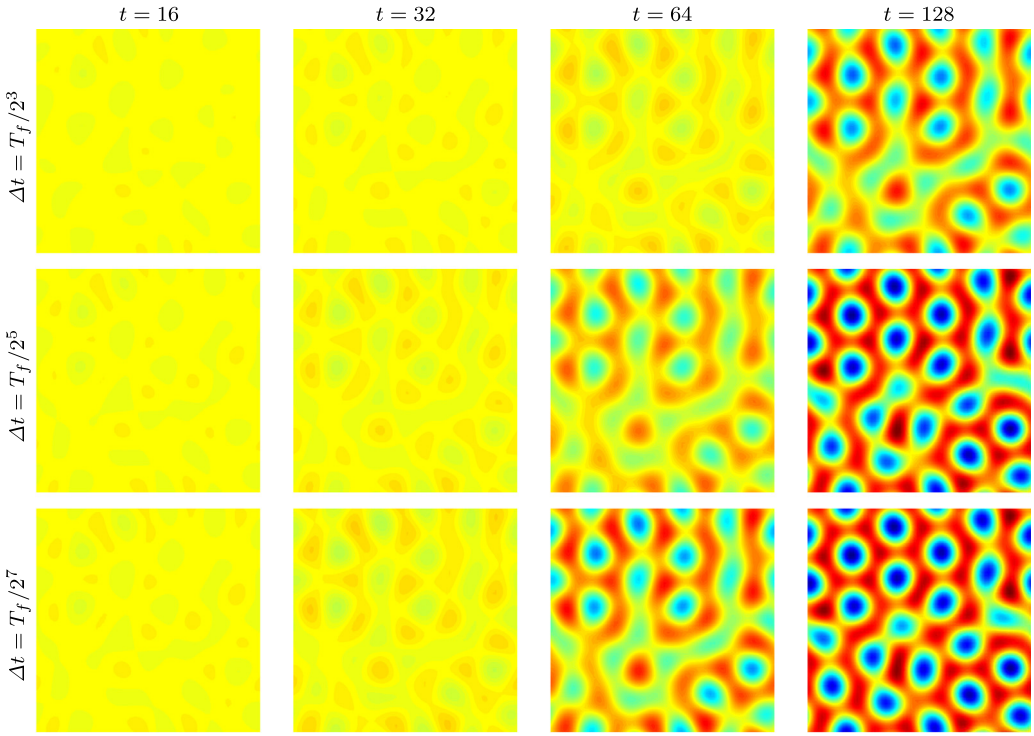

Fig. 8. Solution evolutions with the first-order method for various time steps.

Fig. 8 shows the time evolutions of the density field ϕ using time steps of various sizes Δt computed by the first-order method. As shown previously [7], for the first-order method, evolutions with relatively large time steps cannot reach the reference solutions in the same numerical times.

Fig. 9 shows the time evolutions with the second- and third-order methods for a large time step $\Delta t = T_f/2^3$. Compared to Fig. 8, the higher order methods yield appropriate numerical evolutions even though a large time step is used.

3.3. Dependence of pattern formation on various $\bar{\phi}$ and ϵ

In this section, we introduce an indicator function of the solution ϕ as

$$\Lambda(\phi) = \frac{\int_\Omega \left|\phi - \bar{\phi}\right| d\mathbf{x}}{\int_\Omega \left|\nabla\left(\phi - \bar{\phi}\right)\right| d\mathbf{x}} \tag{37}$$

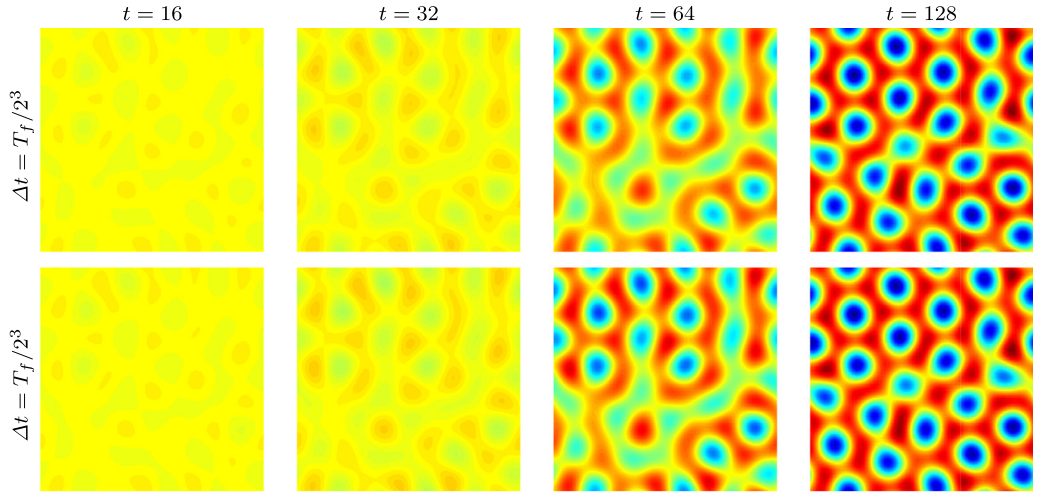

Fig. 9. Solution evolutions with the second- and third-order methods, shown in the upper and lower rows, respectively.

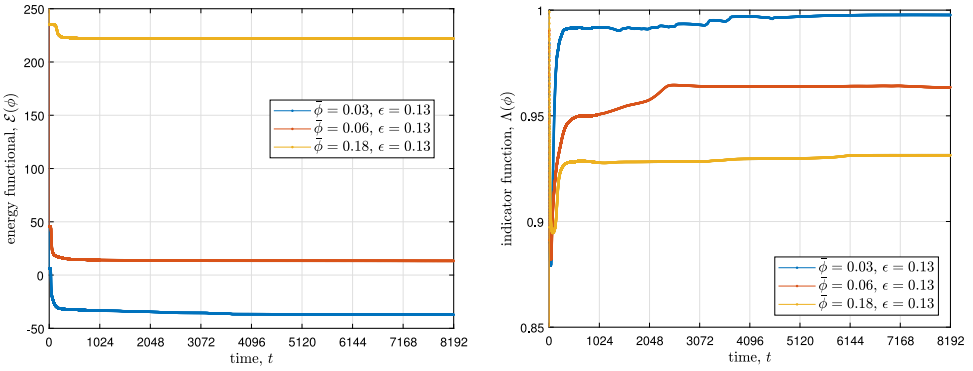

Fig. 10. Evolution of energy functional $\mathcal{E}(\phi)$ and indicator function $\Lambda(\phi)$.

to characterize the pattern formation of the solutions as striped, hexagonal, or homogeneous. For the numerical simulation, we set the randomly perturbed initial condition

$$\phi(x, y, 0) = \bar{\phi} + 0.03 \cdot \text{rand}(x, y) \tag{38}$$

on the domain $\Omega = [0, 128] \times [0, 128]$ with the periodic boundary condition. The numerical solution was evolved to time $T_f = 8192$ with a uniform grid $\Delta x = \Delta y = 1/2$. For moderate accuracy, we employed the second-order method, CSRK-$\mathbf{R}_2(4/5)$. We improved the efficiency of the numerical computations by initially using a small time step $\Delta t = 1/4$ in the earlier stage ($t \leq 1024$), after which we converted this to a larger time step $\Delta t = 4$. We remark that time step size could be further adjusted. A simple and efficient strategy for a pth order adaptive scheme might be choosing Δt_{adap} for the next time step close to

$$\left(\frac{\Delta t_{adap}}{t^{n+1} - t^n}\right)^{p-1} \approx \frac{Tolerance\ Limit}{T_f} \frac{t^{n+1} - t^n}{\|\phi^{n+1} - \phi^n\|},$$

which could be easily coupled with the RK method.

Fig. 10 shows the evolution of the energy functional $\mathcal{E}(\phi)$ and indicator function $\Lambda(\phi)$ for various average densities $\bar{\phi} = 0.03, 0.06, 0.18$ for a constant value of epsilon $\epsilon = 0.13$. All the results seem to evolve to the specific values for each parameter set and the solutions stabilize at $t = T_f$.

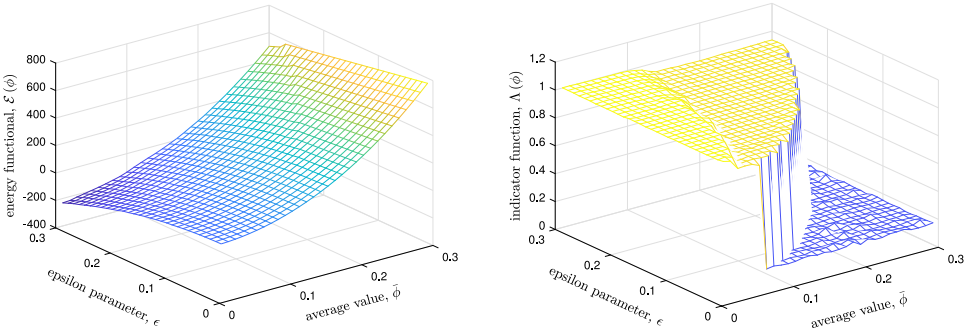

Fig. 11. Distribution of energy functional $\mathcal{E}(\phi)$ and indicator function $\Lambda(\phi)$ for the solution of $\phi(\cdot, T_f)$ with various parameters of $\bar{\phi}$ and ϵ.

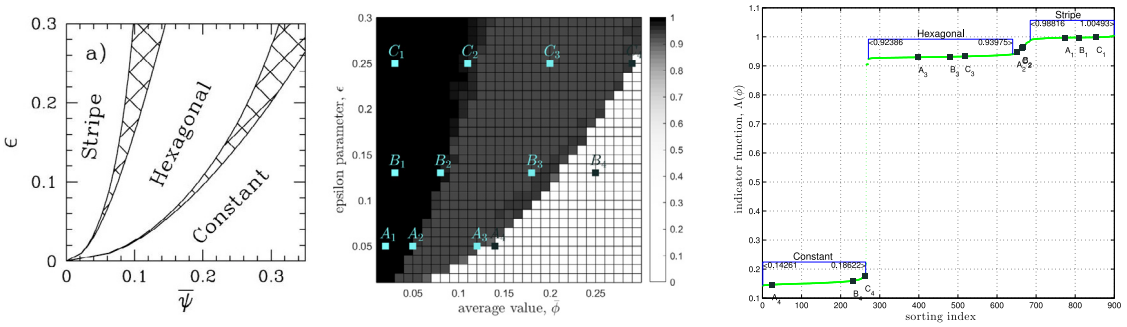

Fig. 12. (a) Phase diagram (Reprinted with permission from [4]). Here, $\bar{\psi}$ is the average value which is identical to $\bar{\phi}$. (b) Values of $\Lambda(\phi(\cdot, T_f))$ for 30×30 parameter sets of $\bar{\phi}$ and ϵ. The black, gray, and white regions indicate $\Lambda(\phi) = 1$, 0.75, and 0, respectively. (c) Sorted values of the indicator function $\Lambda(\phi(\cdot, T_f))$ in (b).

Fig. 11 shows the mesh plots for the value of $\mathcal{E}(\phi)$ and $\Lambda(\phi)$ with respect to $\bar{\phi}$ and ϵ at the final time $t = T_f$. We consider a domain for the parameters as $(\bar{\phi}, \epsilon) \in (0, 0.3] \times (0, 0.3]$ and uniform spacing with $\Delta\bar{\phi} = \Delta\epsilon = 0.01$. Unlike the smooth distribution of the energy, the result for the indicator shows a step-like profile.

Fig. 12(a) shows a phase diagram that is described in [4] by the linearized theory and (b) shows the checkerboard plot for the same result of $\Lambda(\phi)$ in Fig. 11. The different regions of the phase diagram can be compared by using the value of the indicator function (37) to characterize the pattern formation. Fig. 12(c) displays the 30×30 indicator values in ascending order and it indicates that each pattern intends to be in a certain range of values. The range of the values for the stripe cases (A_1, B_1, C_1) is in 0.98816 to 1.00493, the hexagonal cases (A_3, B_3, C_3) in 0.92386 to 0.93975, and the constant case (A_4, B_4, C_4) in 0.14261 to 0.18622. The square dots in Fig. 12(b) and (c) are the parameter set for the solutions in Fig. 13.

Fig. 13 shows the numerical solutions at the final time $t = T_f$. The specific parameters $\bar{\phi}$ and ϵ are written above each figure and they are indicated in Fig. 12(b) by solid squares. To enable the magnitude of the solutions to be compared, we assign the color levels for the red, green, and blue regions as $\phi = 1$, 0, and -1, respectively. In general, as the parameter ϵ increases, from the bottom row to the top row, the magnitude of the solutions increases. On the other hand, the formation of patterns consisting of stripes, which evolve into hexagons, and finally into a constant pattern is clearly demonstrated when observing the columns from left to right. Furthermore, the snapshots in the second column show the coexistence of striped and hexagonal patterns.

4. Conclusions

We proposed high-order methods that guarantee the decreasing property of the energy functional by employing the Convex Splitting Runge–Kutta method and provided detailed proof of mass conservation, unconditional

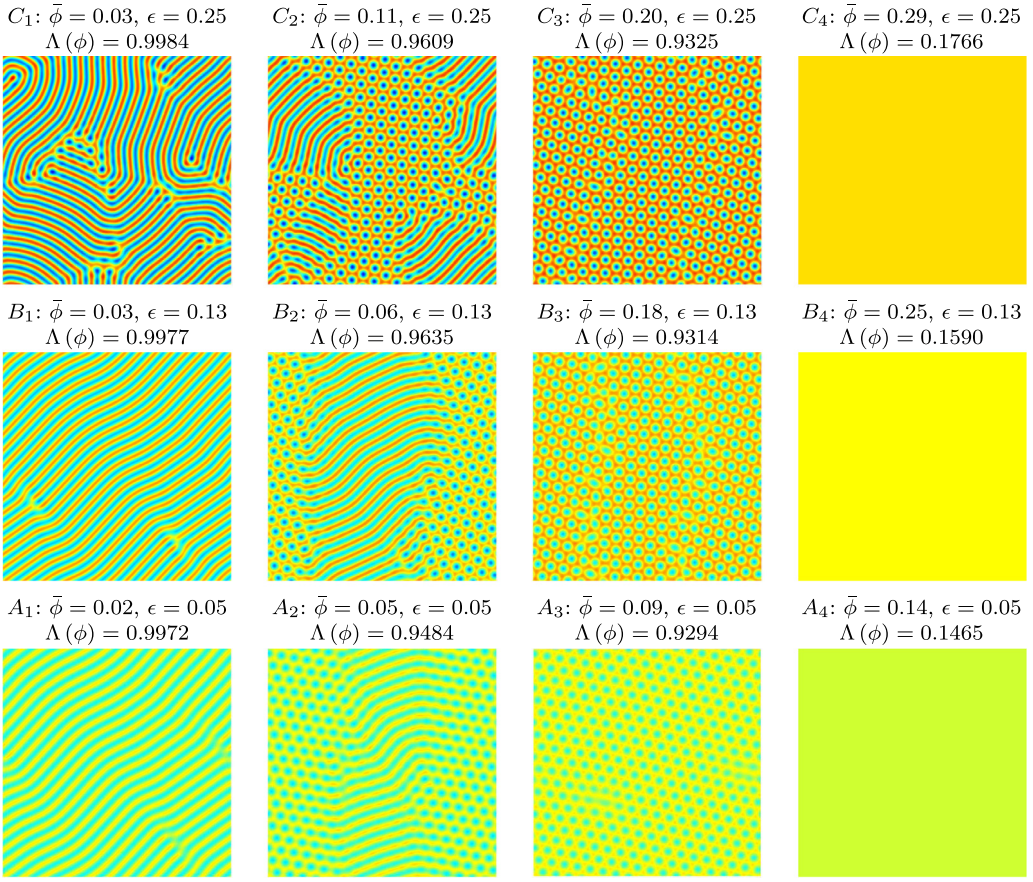

Fig. 13. Solutions $\phi\left(x, y, T_f\right)$ with various parameters $\bar{\phi}$ and ϵ. (For interpretation of the references to color in this figure legend, the reader is referred to the web version of this article.)

energy stability, and unique solvability for the phase-field crystal equation. We presented one complete family of parameters of the second-order methods and selected examples of third-order methods. Various numerical experiments demonstrated that energy stability could be attained with the desired time accuracy and we proposed an indicator function to characterize the pattern formation for long-time simulation. For a long time simulation, time step size can be chosen adaptively which could be easily coupled with the RK method. We showed the effectiveness of the second and third Convex Splitting Runge–Kutta methods for the phase-field crystal equation; however, a best choice selection of Runge–Kutta coefficients for the numerical simulation of a particular equation would require further investigation.

Acknowledgment

This research was supported by Basic Science Research Program through the National Research Foundation of Korea (NRF) funded by the Korean government (2017R1D1A1B0-3032422, 2017R1E1A1A0-3070161, 2019R1C1C1-011112, 2019R1A6A1A1-1051177).

References

[1] S.M. Allen, J.W. Cahn, A microscopic theory for antiphase boundary motion and its application to antiphase domain coarsening, Acta Metall. 27 (6) (1979) 1085–1095.
[2] J.W. Cahn, J.E. Hilliard, Free energy of a nonuniform system. I. Interfacial free energy, J. Chem. Phys. 28 (2) (1958) 258–267.
[3] J. Swift, P.C. Hohenberg, Hydrodynamic fluctuations at the convective instability, Phys. Rev. A 15 (1) (1977) 319.
[4] K. Elder, M. Katakowski, M. Haataja, M. Grant, Modeling elasticity in crystal growth, Phys. Rev. Lett. 88 (24) (2002) 245701.

[5] K. Elder, M. Grant, Modeling elastic and plastic deformations in nonequilibrium processing using phase field crystals, Phys. Rev. E 70 (5) (2004) 051605.
[6] D.J. Eyre, An unconditionally stable one-step scheme for gradient systems, 1998, Unpublished article.
[7] Z. Hu, S.M. Wise, C. Wang, J.S. Lowengrub, Stable and efficient finite-difference nonlinear-multigrid schemes for the phase field crystal equation, J. Comput. Phys. 228 (15) (2009) 5323–5339.
[8] J. Shin, H.G. Lee, J.-Y. Lee, First and second order numerical methods based on a new convex splitting for phase-field crystal equation, J. Comput. Phys. 327 (2016) 519–542.
[9] Y. Li, J. Kim, An efficient and stable compact fourth-order finite difference scheme for the phase field crystal equation, Comput. Methods Appl. Mech. Engrg. 319 (2017) 194–216.
[10] P. Vignal, L. Dalcin, D.L. Brown, N. Collier, V.M. Calo, An energy-stable convex splitting for the phase-field crystal equation, Comput. Struct. 158 (2015) 355–368.
[11] K. Glasner, S. Orizaga, Improving the accuracy of convexity splitting methods for gradient flow equations, J. Comput. Phys. 315 (2016) 52–64.
[12] X. Yang, D. Han, Linearly first- and second-order, unconditionally energy stable schemes for the phase field crystal model, J. Comput. Phys. 330 (2017) 1116–1134.
[13] Z. Zhang, Y. Ma, Z. Qiao, An adaptive time-stepping strategy for solving the phase field crystal model, J. Comput. Phys. 249 (2013) 204–215.
[14] H. Gomez, X. Nogueira, An unconditionally energy-stable method for the phase field crystal equation, Comput. Methods Appl. Mech. Engrg. 249 (2012) 52–61.
[15] H.G. Lee, J. Shin, J.-Y. Lee, First- and second-order energy stable methods for the modified phase field crystal equation, Comput. Methods Appl. Mech. Engrg. 321 (2017) 1–17.
[16] S.M. Wise, C. Wang, J.S. Lowengrub, An energy-stable and convergent finite-difference scheme for the phase field crystal equation, SIAM J. Numer. Anal. 47 (3) (2009) 2269–2288.
[17] J. Shin, H.G. Lee, J.-Y. Lee, Convex Splitting Runge–Kutta methods for phase-field models, Comput. Math. Appl. 73 (11) (2017) 2388–2403.
[18] C. Kennedy, M. Carpenter, Additive Runge–Kutta schemes for convection-diffusion-reaction equations, Appl. Numer. Math. 44 (1-2) (2003) 139–181.
[19] E. Zharovsky, A. Sandu, H. Zhang, A class of implicit-explicit two-step Runge–Kutta Methods, SIAM J. Numer. Anal. 53 (1) (2015) 321–341.
[20] L. Pareschi, G. Russo, Implicit-explicit Runge–Kutta schemes for stiff systems of differential equations, Recent Trends Numer. Anal. 3 (2000) 269–289.
[21] J. Shin, H.G. Lee, J.-Y. Lee, Unconditionally stable methods for gradient flow using Convex Splitting Runge–Kutta scheme, J. Comput. Phys. 347 (2017) 367–381.